

Behavior of the Position and Ellipticity Angles at Polarization Mode Transitions in Pulsar Radio Emission

M. M. MCKINNON¹

¹*National Radio Astronomy Observatory, Socorro, NM 87801 USA*

ABSTRACT

Polarization observations of radio pulsars show that abrupt transitions in the polarization vector's position angle can be accompanied by large excursions in the vector's ellipticity angle, suggesting the vector passes near the right or left circular pole of the Poincaré sphere. The behavior of the angles can be explained by a transition in dominance of the orthogonal polarization modes or a vector rotation caused by a change in the phase difference between the modes. Four polarization models are examined to quantify and understand the behavior of the angles at a mode transition: coherent polarization modes, partially coherent modes, incoherent modes with nonorthogonal polarization vectors, and incoherent orthogonal modes with an elliptically polarized emission component. In all four models, the trajectory of the mode transition on the Poincaré sphere follows the geodesic that connects the orientations of the mode polarization vectors. The results from the models can be similar, indicating that the interpretation of an observed transition within the context of a particular model is not necessarily unique. The polarization fraction of the emission and the average ellipticity angle depend upon the statistical character of the mode intensity fluctuations. The polarization fraction increases as the fluctuations increase. The excursion in ellipticity angle can be large when the mode intensities are quasi-stable and is suppressed when the intensity fluctuations are large.

1. INTRODUCTION

Polarization observations of radio pulsars show that the position angle (PA) of the emission's polarization vector can change discontinuously by 90°, indicating the emission is comprised of two modes of orthogonal polarization (OPMs; Manchester, Taylor, & Huguenin 1975; Cordes, Rankin, & Backer 1978). The modes are generally attributed to the natural modes of wave propagation in the pulsar magnetosphere (Melrose 1979; Allen & Melrose 1982; Barnard & Arons 1986). Statistical summaries of single-pulse polarization observations (e.g., Backer & Rankin 1980; Stinebring et al. 1984, hereafter S84) show the PAs of the two modes can follow parallel tracks across the pulse that are offset from one another by about 90°, with both tracks following the classic rotating vector model (RVM) of Radhakrishnan & Cooke (1969). However, the observations also show that angular separations between the two mode peaks in PA histograms can be less than 90°. Backer & Rankin

Corresponding author: M. M. McKinnon

mmckinn@nrao.edu

(1980) noted that approximately half of the stars they observed at 430 MHz had mode PA separations of less than 90° . S84 observed many of the same stars at 1404 MHz and found the PA separations were closer to 90° , suggesting the PA separations are frequency-dependent. Additionally, the observed shape and extent of a PA transition can deviate from what is expected from a change in the dominant polarization mode. The transition is instantaneous and discontinuous over 90° if the OPMs are incoherent, but many transitions change gradually with pulse longitude, and the total change in PA over the duration of the transition can be less than 90° (e.g., see PSR B0809+74 in Figure 2 of Edwards (2004)). To explain the observed behavior of the PA, S84 suggested the emission is comprised of incoherent OPMs and an independent, linearly polarized component.

More recent polarization observations of single pulses have reported measurements of the emission's ellipticity angle (EA). Some changes in the EA observed at PA transitions are unusual and also deviate from what is expected from a change in the dominant polarization mode. Ideally, the EA should change discontinuously by $\Delta\chi = 2\chi_o$ at an incoherent OPM transition, where χ_o is the EA of one polarization mode and $-\chi_o$ is the EA of the other mode. The observed change in the EA, however, can be large, occasionally approaching $\Delta\chi = \pm 45^\circ$. For example, the observation of PSR B0329+54 by Edwards & Stappers (2004, hereafter ES04) reveals a large excursion in the EA at the pulsar's leading outrider (see their Figure 1). The mean EA abruptly decreases from $\chi \simeq 0^\circ$ to $\chi \simeq -35^\circ$ via an asymmetric discontinuity, indicating the polarization vector passes near the left circular pole of the Poincaré sphere. The mean PA at the EA excursion changes discontinuously by about 90° , as one might expect at a transition between incoherent OPMs. Other PA transitions on the leading edge of the pulsar's central component and in its trailing outrider are more gradual in pulse longitude, and the total change in PA over the transitions appears to fall short of the expected 90° . These PA transitions are generally accompanied by inflections in the EA. The EA inflection points are not as prominent or distinct as the feature in the pulsar's leading outrider, and the total change in EA at the transitions is $\Delta\chi < 45^\circ$. In the pulsar's central component, the average EA forms a broad asymmetric feature that extends toward the right circular pole of the Poincaré sphere. The average PA changes gradually at this location, but does not bridge the well-defined PA traces of the individual polarization modes. In Figure 2 of ES04, individual samples of the PA and EA form a partial annulus in one hemisphere of the Poincaré sphere and a compact ellipse at the center of the other hemisphere. To explain the abrupt EA excursion observed in the pulsar, ES04 suggested the emission is comprised of incoherent OPMs and an independent, circularly polarized component. They also suggested the EA excursion could be caused by incoherent modes with polarization vectors that are not strictly orthogonal. Departures from orthogonality could arise from differential refraction of the polarization modes (Cheng & Ruderman 1979; Barnard & Arons 1986; Petrova 2001; McKinnon 2003, hereafter M03; Oswald et al. 2023b, hereafter OKJ).

Dyks (2020, hereafter D20) noted the polarization modes may be coherent and recognized that an EA excursion could be produced by a rotation of the polarization vector about the Poincaré sphere. The rotation is caused by a change in the phase offset between the polarization modes. For some vector geometries and rotations, the associated change in PA is gradual and its total change is less than 90° . Dyks, Weltevrede, & Ilie (2021, hereafter DWI) documented the coherent mode model and showed that an EA excursion could also be produced by altering the ratio of the amplitudes of the modes' electric fields. The trajectory of this mode transition follows a great circle on the Poincaré

sphere that is offset from the left or right circular pole by an angle determined by the phase offset between the modes. The PA in this case changes gradually over 90° .

Oswald et al. (2023a) conducted a comprehensive analysis of 271 pulsars to identify associations between their polarization properties. They found links between PA behavior that deviated from the RVM, the frequency evolution of the polarization, and the presence of circular polarization features. They suggested the links could be explained by propagation effects in the magnetosphere and proposed that the polarization modes were partially coherent. OKJ documented the partially coherent model and used it to show that observed changes in the EA were consistent with a vector rotation in two pulsars and a change in the ratio of mode intensities in another.

In summary, a variety of models have been proposed to explain the behavior of the polarization angles at a mode transition. An in-depth examination of the models is warranted, to quantify the predicted behavior of the angles and to ascertain the applicability of the models. Four polarization models are examined and compared in this paper: coherent polarization modes (DWI), partially coherent modes (OKJ), incoherent modes with nonorthogonal polarization vectors (M03, ES04), and a combination of incoherent OPMs with an elliptically polarized emission component (S84, ES04). Henceforth, the models are designated, respectively, as the COH model, the PCOH model, the NPM model, and the EPC model. The NPM and EPC models are variants of a statistical model of pulsar polarization developed by McKinnon & Stinebring (1998, hereafter MS).

The paper is organized as follows. The basis for evaluating the models is outlined in Section 2. The NPM model is presented in Section 3, and the EPC model is presented in Section 4. The COH and PCOH models are reviewed in Section 5. The behaviors of the PA, EA, and polarization fraction at a mode transition are derived in each case. The properties of the models are compared in Section 6. The polarization fraction and average EA depend upon the statistical character of the mode intensity fluctuations. The effects of different types of mode intensity fluctuations upon the polarization fraction and average EA are illustrated in Section 7. The NPM model is used in both a numerical simulation of a mode transition and the derivation of the eigenvalues and eigenvectors of the Stokes QUV covariance matrix. Section 8 reviews the change in EA caused by a rotation of the polarization vector and suggests potential applications of the models to select pulsars. Summary comments are listed in Section 9. The appendices provide supporting information for the analysis. Appendix A lists the equations for the measured EA when the intensities of the incoherent OPMs are Erlang or Gaussian random variables (RVs). The eigenvectors determined from the NPM model are compared to the mode polarization vectors in Appendix B.

2. DEFINITIONS AND BASIS OF MODEL EVALUATION

For the purpose of evaluating the models, a mode transition is defined as a change in the relative mean intensities of the polarization modes that results in a change in the dominant mode. The mode transition causes the PA to change by $\Delta\psi \leq \pi/2$. A rotation of the polarization vector can also change the PA and EA, but it is not a mode transition as defined here (see Section 8.1). A mode transition so defined can be described in more detail with a simple model of incoherent OPMs. The MS statistical model of pulsar polarization assumes the emission consists of two independent, simultaneously occurring, completely polarized orthogonal modes. The model treats the mode intensities as RVs, X_A and X_B , to account for the emission's variability and the polarization's tendency to switch randomly between orthogonally polarized states. With these assumptions, the intensity of the combined radiation is the sum of the RVs, and its polarization is related to their difference. The

instantaneous values of the Stokes parameters I, Q, U, and V at a given pulse longitude are (e.g., M24):

$$I = X_A + X_B \quad (1)$$

$$Q = \cos(2\psi_o) \cos(2\chi_o)(X_A - X_B) \quad (2)$$

$$U = \sin(2\psi_o) \cos(2\chi_o)(X_A - X_B) \quad (3)$$

$$V = \sin(2\chi_o)(X_A - X_B), \quad (4)$$

where ψ_o is the PA of the mode A polarization vector and χ_o is its EA. A mode transition in a pulsar's average profile is presumably caused by changes in the physical processes that excite the two modes. These changes imply the ratio of the mode mean intensities, $M = \langle X_A \rangle / \langle X_B \rangle$, changes with pulse longitude to effect the transition. McKinnon (2022, 2024; hereafter M22, M24) introduced a parameter, m , that is related to the polarization fraction of the radiation. It is defined by

$$m = \frac{\langle X_A \rangle - \langle X_B \rangle}{\langle X_A \rangle + \langle X_B \rangle} = \frac{M - 1}{M + 1}, \quad -1 \leq m \leq 1. \quad (5)$$

The radiation is comprised solely of mode A when $m = 1$ ($M = \infty$) and is comprised solely of mode B when $m = -1$ ($M = 0$). The mode transition occurs at $m = 0$ ($M = 1$). Changes in m , or M , with pulse longitude drive the transition between the modes. Since m must change sufficiently to complete the transition, it may be viewed as a proxy for pulse longitude over the duration of the transition (M24). Although the parameter m originated in an incoherent OPM model, it is applicable in the COH and PCOH models, as shown in Section 5.

The measured PA is related to the azimuth of the polarization vector in the Poincaré sphere and is defined by

$$\psi = \frac{1}{2} \arctan \left(\frac{\langle U \rangle}{\langle Q \rangle} \right), \quad (6)$$

where the angular brackets denote an average over multiple pulses at a given pulse longitude. A transition in the PA of $\Delta\psi = \pi/2$ occurs when the mode mean intensities are equal to one another, $\langle X_A \rangle = \langle X_B \rangle$ (i.e., when $\langle Q \rangle = 0$). The measured EA is related to the latitude of the polarization vector and is defined by

$$\chi = \frac{1}{2} \arctan \left(\frac{\langle V \rangle}{\langle L \rangle} \right), \quad (7)$$

where $\langle L \rangle = \langle (Q^2 + U^2)^{1/2} \rangle$ is the mean linear polarization. Both the PA and EA are determined by ratios of the Stokes parameters, and since the Stokes parameters are determined by the mode intensities, the PA and EA are functions of m . The polarization models can then be compared against one another by comparing the variations of their PAs and EAs with m . The models are characterized by multiple parameters, but m is the only parameter that is common to all four models. The analysis assumes the other parameters remain fixed over the duration of the mode transition.

A direct comparison between the models can be complicated by different geometries assumed for the orientations of the mode polarization vectors. Fortunately, the vector geometries in MS, DWI, and OKJ are the same. The mode vectors reside along the Stokes Q-axis of the Poincaré sphere in each model. Therefore, the equations for the Stokes parameters in the models can be compared directly without further modification, apart from a normalization for consistency in units between models.

3. INCOHERENT MODES WITH NONORTHOGONAL POLARIZATION VECTORS

The NPM model is the MS statistical model modified to account for mode polarization vectors that are not strictly orthogonal. Departures from orthogonality in linear and circular polarization are evaluated separately prior to deriving a general result.

3.1. *Change in the PA at an Incoherent NPM Transition*

The geometry used to determine how the measured PA is affected by a nonorthogonality in the linear component of the mode polarization vectors is shown in panel (a) of Figure 1. The geometry assumes the EAs of both modes are equal to zero, so that the vectors reside in the Q-U plane of the Poincaré sphere. The PA of the mode A vector is $\psi_A = 0$, and the PA of the mode B vector is $\psi_B = \pi/2 - \delta_L$, where the constant angle δ_L represents the departure from orthogonality in linear polarization. Following the analysis originally outlined in M03, the mean values of the Stokes parameters Q and U from the geometry in the figure are

$$\langle U \rangle = \langle X_B \rangle \sin(2\delta_L), \quad (8)$$

$$\langle Q \rangle = \langle X_A \rangle - \langle X_B \rangle \cos(2\delta_L). \quad (9)$$

By substituting the ratio of the mode mean intensities, $M = \langle X_A \rangle / \langle X_B \rangle$, with the parameter m as defined by Equation 5, the PA can be shown to vary with m according to

$$\psi(m) = \frac{1}{2} \arctan \left[\frac{\tan \delta_L (1 - m)}{\tan^2 \delta_L + m} \right]. \quad (10)$$

Equation 10 is shown in panel (b) of Figure 1. The transition occurs at $m_t = -\tan^2 \delta_L$, where the PA is $\psi = \pi/4$. The PA is antisymmetric about $m = 0$, where $\psi = \pi/4 - \delta_L/2$. The total change in PA across the NPM transition is $\Delta\psi = \pi/2 - \delta_L$.

The rate at which the PA changes with m is

$$\frac{d\psi}{dm} = -\frac{1}{2} \frac{\tan \delta_L}{(\tan^2 \delta_L + m^2)}. \quad (11)$$

The rate is symmetric about $m = 0$, where the PA changes at the maximum rate of $-1/(2 \tan \delta_L)$. The rate at the mode transition is slightly less, at $-\cos^2 \delta_L / (2 \tan \delta_L)$. The rates at $m = \pm 1$ are both equal to $-\sin(2\delta_L)/4$.

3.2. *Change in the EA at an Incoherent NPM Transition*

The geometry used to determine how the measured EA is affected by a nonorthogonality in the circular component of the polarization vectors is shown in panel (c) of Figure 1. The geometry

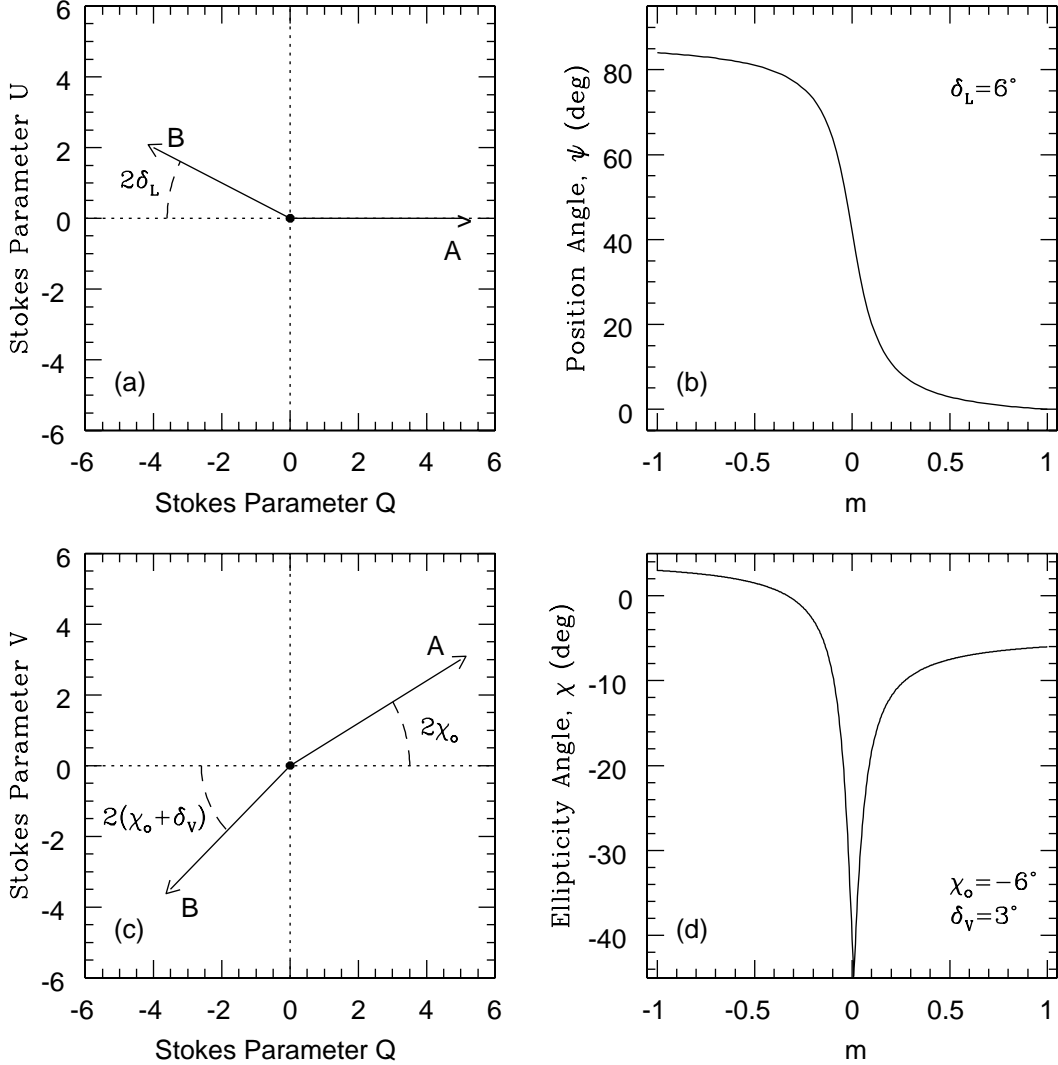


Figure 1. Geometry of the mode polarization vectors when they are not orthogonal, and the resulting change in the PA and EA at a transition between the polarization modes. Panel (a) shows the geometry of the vectors when their linear components are not orthogonal. Panel (b) shows the resulting change in the PA at a mode transition (Equation 10) when $\delta_L = 6^\circ$. Panel (c) shows the geometry of the vectors when their circular components are not orthogonal. Panel (d) shows the resulting change in the EA at a mode transition (Equation 14) when $\chi_o = -6^\circ$ and $\delta_V = 3^\circ$.

assumes the PAs of modes A and B are 0 and $\pi/2$, respectively, so that the mode vectors reside in the Q-V plane of the Poincaré sphere. The EA of the mode A vector is χ_o , and the EA of the mode B vector is $-(\chi_o + \delta_V)$, where the constant angle δ_V represents the departure from orthogonality in circular polarization. Assuming the mode intensities are fixed at the values A and B for a given pulse longitude, the circular and linear polarization resulting from the geometry shown in the figure are

$$V = A \sin(2\chi_o) - B \sin[2(\chi_o + \delta_V)], \quad (12)$$

$$L = |Q| = |A \cos(2\chi_o) - B \cos[2(\chi_o + \delta_V)]|. \quad (13)$$

By further assuming the mode intensities can vary between pulse longitudes, and substituting the ratio of the fixed mode intensities, $M = A/B$, with the parameter m , the EA can be shown to vary with m across the NPM transition according to

$$\chi(m) = \frac{1}{2} \arctan \left[\frac{m \tan(2\chi_o + \delta_V) - \tan \delta_V}{|\tan(\delta_V) \tan(2\chi_o + \delta_V) + m|} \right]. \quad (14)$$

Equation 14 is shown in panel (d) of Figure 1. The EA transition occurs at $m_t = -\tan(\delta_V) \tan(2\chi_o + \delta_V)$, where the EA is $\chi = -\pi/4$. The polarization vector passes through the left circular pole of the Poincaré sphere at that value of m , because the nonorthogonality has introduced a negative component to V that dominates the polarization. The EA excursion is asymmetric about the transition, being broader to the right of the transition than to the left of it. The width, w , of the discontinuity at $\chi = -\pi/8$, where $\tan(2\chi) = -1$, is

$$w = \frac{2 \tan \delta_V}{\cos[2(2\chi_o + \delta_V)]}. \quad (15)$$

The excursion widens as either or both of δ_V or χ_o increase. The circular polarization fraction, \bar{V} , attributable to the nonorthogonality can be estimated by setting the mode-intrinsic EA to zero ($\chi_o = 0$):

$$\bar{V} = \frac{V}{I} = -\frac{B \sin(2\delta_V)}{A + B} = -\sin(2\delta_V) \frac{(1 - m)}{2} \quad (16)$$

The circular polarization fraction varies linearly with m across the transition, and is equal to $-\tan \delta_V$ at the transition.

3.3. General Result

The vector geometries shown in Figure 1 can be used to derive the changes in the PA and EA at a mode transition when the departures from mode orthogonality occur in both linear and circular polarization. Assuming $\psi_A = 0$, $\psi_B = \pi/2 - \delta_L$, $\chi_A = 0$, and $\chi_B = +\delta_V$, the dependence of the average PA upon m is

$$\psi(m) = \frac{1}{2} \arctan \left[\frac{K_3(1 - m)}{K_1 + mK_2} \right], \quad (17)$$

where K_1 , K_2 , and K_3 are constants given by $K_1 = 1 - \cos(2\delta_V) \cos(2\delta_L)$, $K_2 = 1 + \cos(2\delta_V) \cos(2\delta_L)$, and $K_3 = \cos(2\delta_V) \sin(2\delta_L)$. The value of m at the transition is

$$m_t = -\frac{K_1}{K_2} = -\frac{1 - \cos(2\delta_V) \cos(2\delta_L)}{1 + \cos(2\delta_V) \cos(2\delta_L)}. \quad (18)$$

The average EA varies with m according to

$$\chi(m) = \frac{1}{2} \arctan \left\{ \frac{\tan(2\delta_V)(1 - m)}{[2(K_1 + m^2K_2)(1 + \tan^2(2\delta_V)) - (1 - m)^2 \tan^2(2\delta_V)]^{1/2}} \right\}. \quad (19)$$

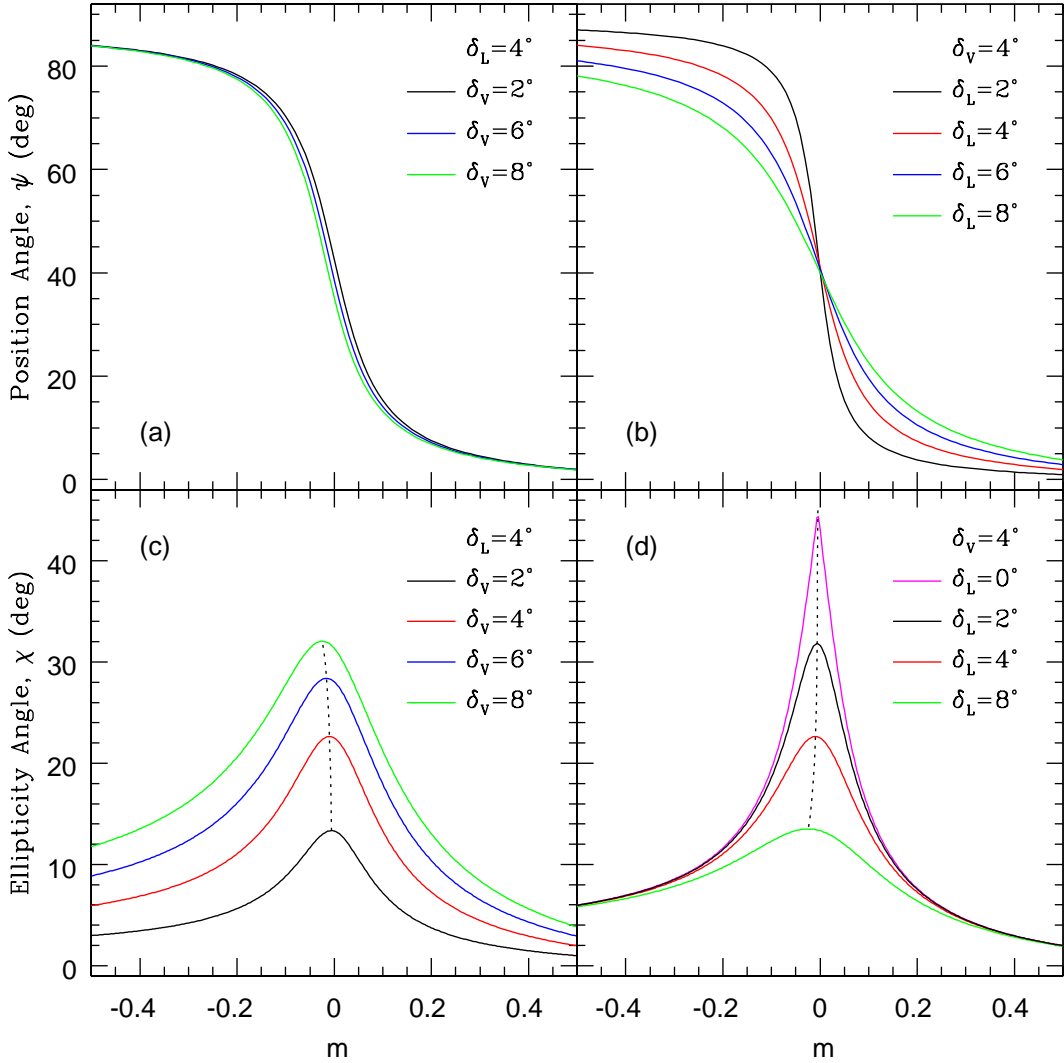


Figure 2. Changes in the PA and EA over a transition between NPMs. Panels (a) and (c) in the left column of the figure show changes in the PA and EA, respectively, for different values of δ_V when δ_L is held constant. Panels (b) and (d) in the right column show changes in the PA and EA, respectively, for different values of δ_L when δ_V is held constant. The dotted black lines in panels (c) and (d) connect the vertices of the transitions' geodesics (Equation 22).

Examples of Equations 17 and 19 are shown in Figure 2. The EA excursion is asymmetric about the transition point, m_t . The slope of the PA transition decreases with increasing values of δ_L . The excursion in the EA increases with increasing δ_V and decreasing δ_L . The EA reaches its peak value of $\chi = \pi/4$ when $\delta_L = 0$. The dotted lines in the lower row of panels denote the peak EA at each mode transition and are discussed in Section 3.4.

If the mode intensities are fixed at a given pulse longitude, but can vary with longitude, the polarization fraction of the NPM model as a function of m is

$$p(m) = (Q^2 + U^2 + V^2)^{1/2}/I = [(K_1 + m^2 K_2)/2]^{1/2}. \quad (20)$$

The fraction is symmetric about $m = 0$, where its minimum value is $p_m = \sqrt{K_1/2}$. The minimum is offset from the mode transition at m_t , where the polarization fraction is $p(m_t) = \sqrt{K_1/K_2}$. For incoherent OPMs ($\delta_L = \delta_V = 0$), the polarization fraction is $p(m) = |m|$.

The derivation of Equation 17 for the average PA assumes the PA of mode A remains constant at zero across the mode transition. If the PA of mode A is constant at some other value (ψ_o), or if it varies linearly, and slowly, with m across the mode transition (e.g., $\psi_o(m) = K_0 m$), the PA is

$$\psi(m) = \frac{1}{2} \arctan \left[\frac{\tan(2\psi_o(m))(K_1 + mK_2) + K_3(1 - m)}{(K_1 + mK_2) - \tan(2\psi_o(m))K_3(1 - m)} \right]. \quad (21)$$

The PA given by Equation 21 varies continuously with m as long as the total change in PA across the transition is $\Delta\psi < \pi/2$. This constraint restricts values of K_0 to $|K_0| < \pi/4$.

3.4. Trajectory of a Mode Transition on the Poincaré Sphere

Projections of the PA and EA, as calculated from Equations 17 and 19, on the Poincaré sphere are shown by the colored lines in Figure 3. The view of the sphere is along its U-axis ($\psi = \pi/4$), with mode A on the sphere equator to the left and mode B on the right. The trajectories of the mode transitions were calculated for different values of δ_L , with δ_V held constant at $\delta_V = 4^\circ$. For each example in the figure, the peak value of the EA occurs at $\psi = \pi/4$ and increases as the value of δ_L decreases. The trajectories follow the geodesics between the orientations of the mode polarization vectors. The orientations of the mode vectors on the sphere and the sphere's origin define a unique plane that intersects the origin. The intersection between the plane and the surface of the sphere is a great circle. The shortest distance between the orientations of the mode vectors on the sphere lies along this great circle and is called the geodesic or great circle distance (GCD; e.g., Kells, Kern, & Bland 1940). The relationship between the PA and EA over the trajectory is given by the equation for the great circle defined by the mode vectors. For the geometry used to derive Equations 17 and 19, the relationship between χ and ψ is

$$\chi(\psi) = \frac{1}{2} \arctan \left[\frac{\sin(2\psi) \tan(2\delta_V)}{\sin(2\delta_L)} \right]. \quad (22)$$

Equation 22 is shown by the open circles in Figure 3 for the values of δ_L and δ_V annotated in the figure. The figure shows that Equation 22 replicates the dependence of χ upon ψ , as determined independently from Equations 17 and 19. The vertex of the geodesic (the peak value of χ) occurs at $\psi = \pi/4$ and is large when δ_V is large and δ_L is small. The vertex is also shown by the black dotted lines in panels (c) and (d) of Figure 2. The dotted lines connect the peak EAs of each example shown in the two panels. When $\delta_V = 0$, the transition trajectory traverses the equator of the Poincaré sphere. When $\delta_L = 0$, the trajectory traverses a meridian of the sphere over one of its poles.

The angular extent, ζ , of the geodesic is the angle subtended by the mode polarization vectors,

$$\zeta = \pi - \arccos[\cos(2\delta_V) \cos(2\delta_L)], \quad (23)$$

which is always less than π . Since the radius of the Poincaré sphere is equal to 1, ζ is also the GCD of the transition trajectory.

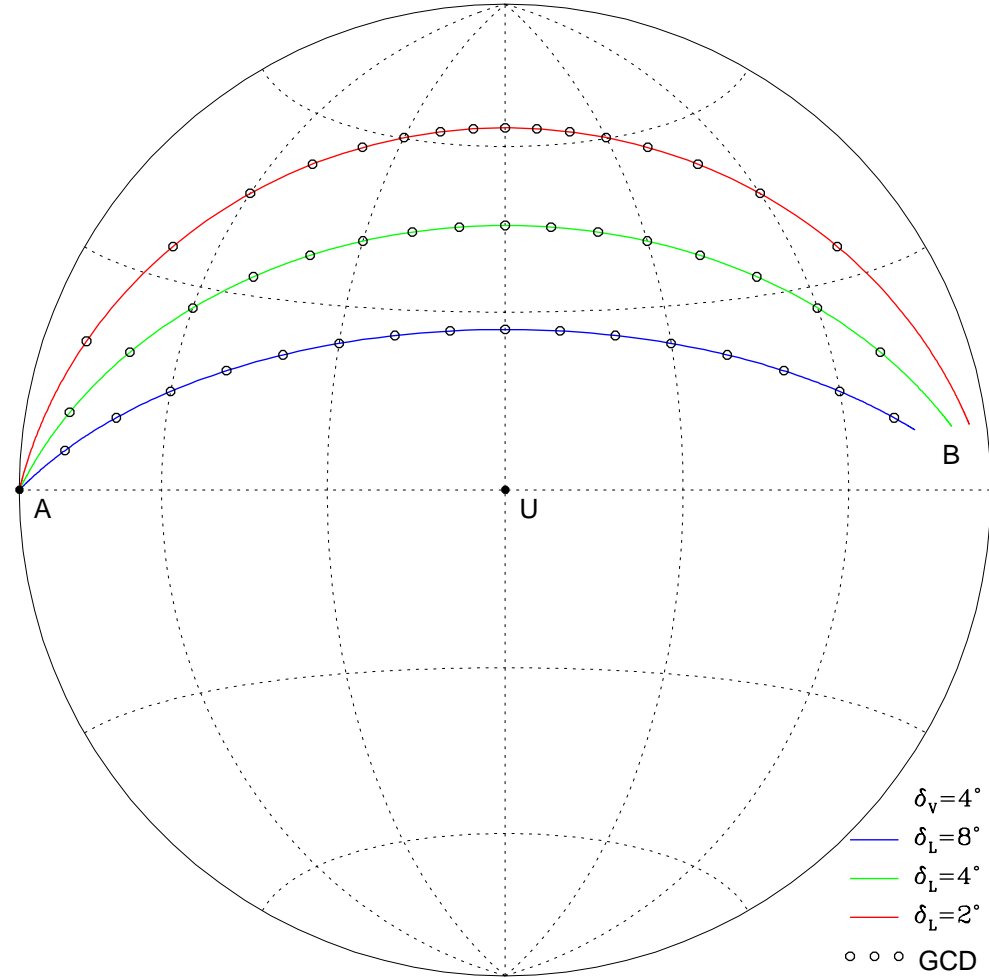


Figure 3. Example trajectories of NPM transitions on the Poincaré sphere. The trajectories (colored lines) are the projections of ψ and χ as determined from Equations 17 and 19, respectively. The values of δ_V and δ_L used to calculate the trajectories are annotated in the figure. The open circles trace the geodesics or GCDs between the orientations of the mode polarization vectors, as calculated from Equation 22. The trajectories follow the geodesics. The view of the sphere is along its U-axis, such that mode A is on the sphere equator at the left, and mode B is at the terminus of each trajectory on the right.

4. INCOHERENT ORTHOGONAL MODES WITH AN ELLIPTICALLY POLARIZED COMPONENT

S84 suggested that a total change in PA of less than $\pi/2$ over a mode transition could be explained by a combination of incoherent OPMs and an independent, linearly polarized emission component. Similarly, ES04 proposed that EA excursions coinciding with PA transitions could be explained by a combination of incoherent OPMs and an independent, circularly polarized component. Both suggestions can be examined by assuming the independent component is elliptically polarized. The

physical origin of the EPC is unknown. The derivations of the PA and EA as functions of m in this case are very similar to those presented in Section 3. The OPMs are assumed to be linearly polarized, and their vectors are assumed to be aligned with the Stokes Q-axis of the Poincaré sphere. The intensity of the EPC is designated as ε , and its PA and EA are denoted by ψ_e and χ_e , respectively. The mode intensities are assumed to be fixed at A and B for a given pulse longitude, and the combined intensity of the three components is assumed to be constant and equal to 1, such that $A + B = 1 - \varepsilon$. The Stokes parameters resulting from these assumptions for the case of $\psi_e = \pi/4$ are

$$Q = A - B, \quad (24)$$

$$U = \varepsilon \cos(2\chi_e), \quad (25)$$

$$V = \varepsilon \sin(2\chi_e). \quad (26)$$

The EPC model is the scenario described by S84 when $\chi_e = 0$ and is the scenario proposed by ES04 when $\chi_e = \pi/4$. The PA and EA derived from the above Stokes parameters are

$$\psi(m) = \frac{1}{2} \arctan \left[\frac{\varepsilon \cos(2\chi_e)}{m(1 - \varepsilon)} \right], \quad (27)$$

$$\chi(m) = \frac{1}{2} \arctan \left\{ \frac{\varepsilon \tan(2\chi_e)}{[m^2(1 - \varepsilon)^2(1 + \tan^2(2\chi_e)) + \varepsilon^2]^{1/2}} \right\}. \quad (28)$$

Examples of Equations 27 and 28 are shown in Figure 4. The mode transition occurs at $m = 0$, where the PA changes at its maximum rate of

$$\frac{d\psi}{dm} = -\frac{(1 - \varepsilon)}{2\varepsilon \cos(2\chi_e)}. \quad (29)$$

The total change in the PA over the transition is $\Delta\psi = \pi/2 - 2\psi_s$, where ψ_s is given by Equation 27 with $m = 1$. The EA excursion is symmetric about $m = 0$, where its peak value is $\chi_p = \chi_e$. The full width of the EA excursion at half its maximum value is

$$w = \frac{2\varepsilon}{1 - \varepsilon} \left(\frac{3 - \tan^2 \chi_e}{1 + \tan^2 \chi_e} \right)^{1/2}. \quad (30)$$

The PA rate increases and the EA excursion narrows as ε decreases and as χ_e increases.

The trajectory of an EPC mode transition also follows a geodesic on the Poincaré sphere. The equation for the great circle that defines the trajectory, and thus the dependence of the EA upon the PA, is

$$\chi(\psi) = \frac{1}{2} \arctan [\sin(2\psi) \tan(2\chi_e)]. \quad (31)$$

The vertex of the EA excursion occurs at $\psi = \pi/4$. The GCD of the trajectory is

$$\zeta = \pi - \arccos \left(\frac{1 - 2\varepsilon}{1 + 2\varepsilon^2 - 2\varepsilon} \right). \quad (32)$$

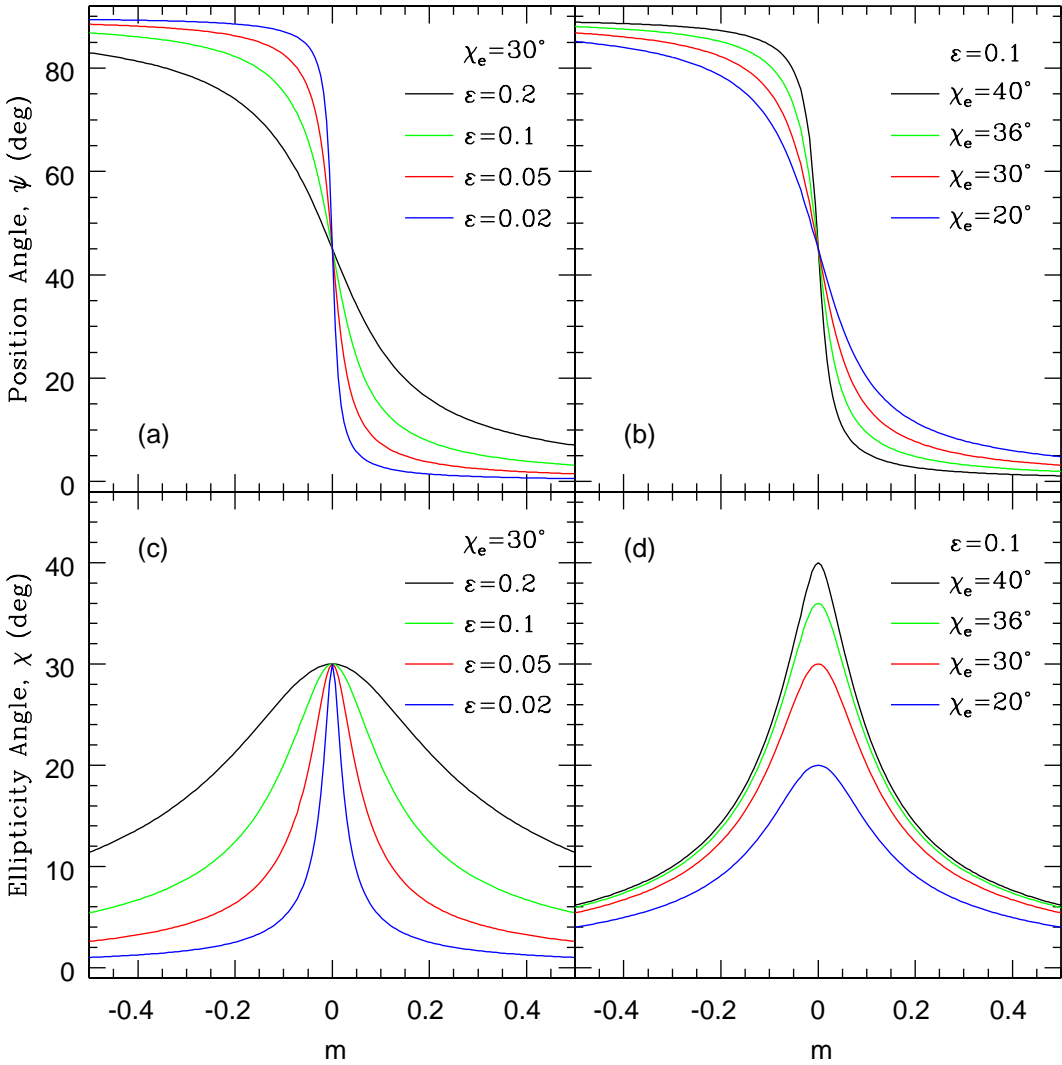


Figure 4. Changes in the PA and EA over a mode transition predicted by the EPC model. Panels (a) and (c) in the left column show the change in the PA and EA for different values of ε when χ_e is held constant. Panels (b) and (d) in the right column of the figure show the change in PA and EA for different values of χ_e when ε is held constant.

The polarization fraction for the EPC model is

$$p(m) = [m^2(1 - \varepsilon)^2 + \varepsilon^2]^{1/2}. \quad (33)$$

The polarization fraction is independent of χ_e and is symmetric about its minimum value of $p_m = \varepsilon$ at $m = 0$.

5. COHERENT AND PARTIALLY COHERENT MODES

The PCOH model developed by OKJ uses three parameters to define the Stokes parameters of the radiation: a coherence factor, C ; a mode strength ratio, R ; and a mode phase offset, η (see their

Equation 5). As OKJ note, the emission produced by partially coherent modes may be interpreted as a combination of coherent and incoherent components. The polarization fraction of the incoherent component is defined by the ratio of OKJ's Stokes parameters Q and I . The ratio is independent of C and η , and is equal, within an immaterial factor of -1, to the parameter m given by Equation 5. OKJ's Stokes parameters U , V , and I determine the polarization fraction of the coherent component. When the coherence factor is $C = 0$, the modes are incoherent, and the PCOH model becomes the MS model of incoherent OPMs. The mode intensity ratio, M , defined in MS is identical to OKJ's mode strength ratio, R . When $C = 1$, the modes are coherent, and the PCOH model is equivalent to the COH model (see Equations 13-15 in DWI). The COH model is characterized by two parameters: a mode mixing angle, ψ_{mx} , and a mode phase lag, δ_{ox} . The phase lag in DWI is the same as the mode phase offset in OKJ, $\eta = \delta_{ox}$, and DWI's mixing angle is related to OKJ's mode strength ratio by

$$\cos(2\psi_{mx}) = \frac{1 - R}{1 + R} = -m. \quad (34)$$

The Stokes parameters defined in DWI and OKJ can be used to derive the dependence of the PA and EA upon m for fixed values of C and η . Using OKJ's notation, the PA and EA are

$$\psi(m) = \frac{1}{2} \arctan \left[\frac{\cos \eta (1 - m^2)^{1/2}}{t(C)m} \right], \quad (35)$$

$$\chi(m) = \frac{1}{2} \arctan \left\{ \tan \eta \left[\frac{1 - m^2}{t^2(C)m^2(1 + \tan^2 \eta) + (1 - m^2)} \right]^{1/2} \right\}, \quad (36)$$

where the factor $t(C) = [(1 - C)^2 + C^2]/C^2$ ranges from $t(1) = 1$ to $t(0) = \infty$. Examples of Equations 35 and 36 are shown in Figure 5. The mode transition occurs at $m = 0$, where the PA changes at its maximum rate of $d\psi/dm = -t(C)/(2 \cos \eta)$. The EA excursion is symmetric about $m = 0$, where its peak value is $\chi_p = \eta/2$. The full width of the EA excursion at half its maximum value is

$$w = 2 \left\{ \frac{3 - \tan^2(\eta/2)}{4 + [t^2(C) - 1][1 + \tan^2(\eta/2)]} \right\}^{1/2}. \quad (37)$$

The PA rate increases and the EA excursion narrows as η increases and as C decreases.

For coherent polarization modes ($C = t(C) = 1$), the PA changes at a maximum rate of $d\psi/dm = -1/(2 \cos(\eta))$. The PA transition can be gradual or discontinuous, although abrupt transitions require $\eta \sim \pi/2$. The EA excursion for the COH model has a width of $w = [3 - \tan^2(\eta/2)]^{1/2}$, and is generally wider than the excursions produced by the PCOH model. The behavior of the polarization angles predicted by the COH model is not shown in a separate figure, but may be inferred from Figure 5 for the PCOH model.

The trajectories of the COH and PCOH mode transitions on the Poincaré sphere follow great circles. The equation for the great circle is

$$\chi(\psi) = \frac{1}{2} \arctan [\sin(2\psi) \tan \eta], \quad (38)$$

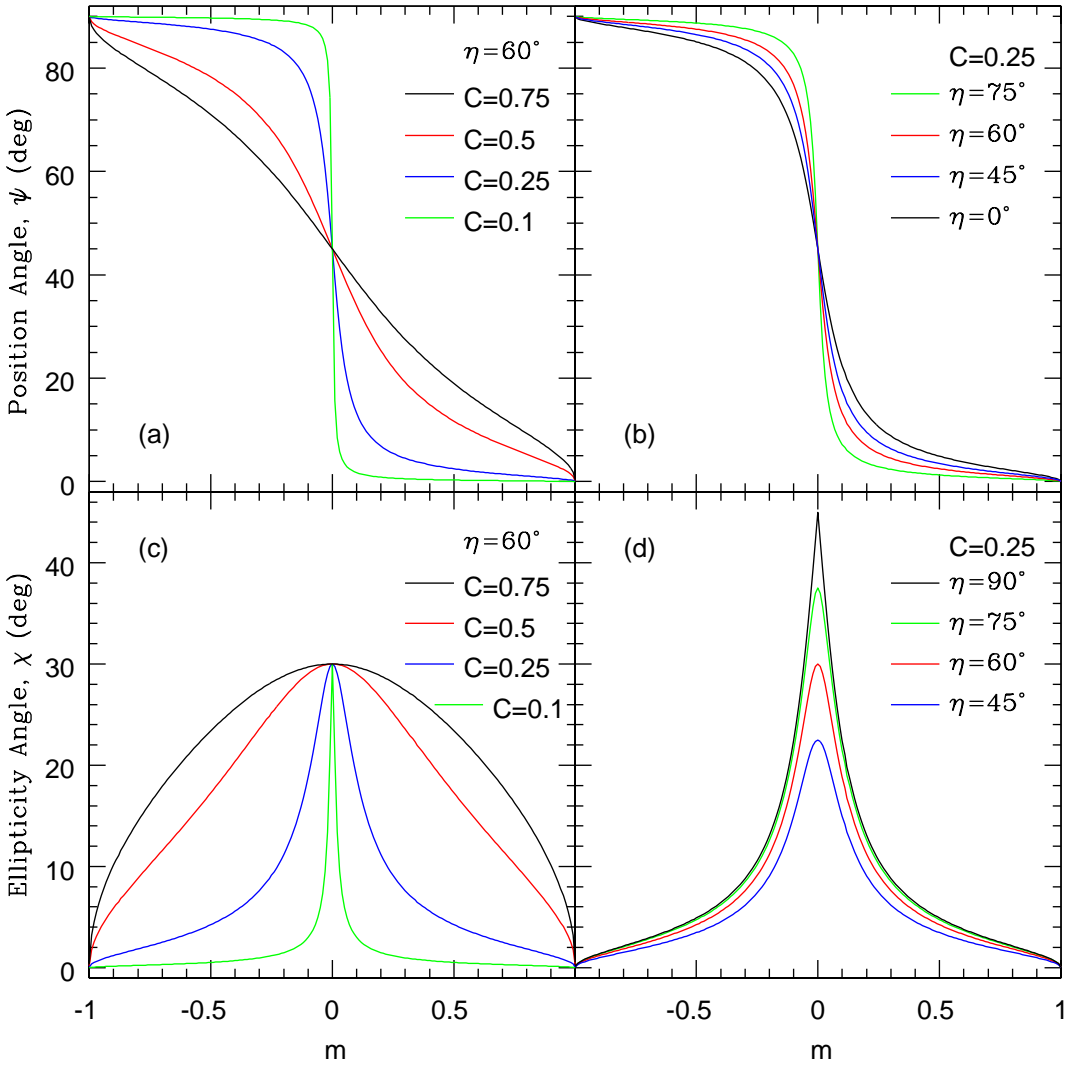


Figure 5. Changes in the PA and EA over a transition between partially coherent polarization modes. Panels (a) and (c) in the left column of the figure show the change in PA and EA, respectively, for different values of C when the phase offset is held constant at $\eta = 60^\circ$. Panels (b) and (d) in the right column of the figure show the change in PA and EA, respectively, for different values of η when the coherence factor is held constant at $C = 0.25$.

and it applies to both coherent and partially coherent modes. The GCD of the trajectory is $\zeta = \pi$, because the mode vectors reside on antipodal points of the Poincaré sphere.

The polarization fraction of the PCOH model figures prominently in OKJ's analysis and interpretation of their observations. The polarization fraction for both the COH and PCOH models is

$$p(m) = [m^2(t^2(C) - 1) + 1]^{1/2}/t(C). \quad (39)$$

Table 1. Comparison of Polarization Model Properties

Model	NPM	EPC	PCOH	COH	ICOH
$\Delta\psi$	$\pi/2 - \delta_L$	$\pi/2 - 2\psi_s$	$\pi/2$	$\pi/2$	$\pi/2$
$\tan(2\chi_p)$	$\tan(2\delta_V)/\sin(2\delta_L)$	$\tan(2\chi_e)$	$\tan\eta$	$\tan\eta$	0
GCD, ζ	$< \pi$	$< \pi$	π	π	π
p_m	$\sqrt{K_1/2}$	ε	$1/t(C)$	1	0
N	3	3	3	2	1

The fraction is independent of the mode phase offset, η , and is symmetric about its minimum value of $p_m = 1/t(C)$ at $m = 0$. For the COH model, the polarization fraction remains constant at $p = 1$ over the transition's duration.

The application of the PCOH model to a mode transition described here is the same procedure used by OKJ to interpret the polarization of PSR J0134-2937 (see their Figure 9). They found that values of C and η were approximately constant with pulse longitude and showed that R , which is related to the parameter m , varied roughly linearly with longitude. As Equation 39 shows, once C is known, the polarization fraction observed over a range of longitudes can provide a direct mapping between m , or R , and longitude.

6. MODEL COMPARISON

The properties of the polarization models are compared in Table 1. For completeness, the properties of a transition between incoherent OPMs (ICOH) have been included in the table. The table entries include the total change in the PA across the mode transition, $\Delta\psi$; the tangent of the peak EA, χ_p ; the GCD of each mode transition, ζ ; the minimum polarization fraction, p_m ; and the number of parameters used to characterize each model, N . The table entries, combined with Figures 2, 4, and 5, show the models have similarities, as well as differences. The PA transition and EA excursion of each model coincide with one another, and their durations are comparable. The PA transitions of the COH model tend to be more gradual and its EA excursions are generally broader than their counterparts in the other models. The PA transition for each model is antisymmetric about $m = 0$; however, the transition point for the NPM model, m_t , does not coincide with $m = 0$. The PA changes discontinuously in a transition in the ICOH model, but changes gradually over a transition in the other models. The total change in the PA over a transition in the PCOH, COH, and ICOH models is $\Delta\psi = \pi/2$ and is less than $\pi/2$ in the NPM and EPC models. In all cases except for the ICOH model, the EA can trace an excursion that originates near the equator of the Poincaré sphere and passes near one of its poles. The ICOH model is not capable of producing an EA excursion. The excursion in the EPC, PCOH, and COH models is symmetric about a transition, but is asymmetric about a transition in the NPM model. The maximum value of the EA within an excursion, χ_p , is determined by the model parameters. For each model, the trajectory of a mode transition on the Poincaré sphere follows the geodesic connecting the orientations of the mode polarization vectors, with the details of the trajectory determined by the model's parameters. In the ICOH model, the orientations of the mode vectors reside at antipodal points of the Poincaré sphere. A unique great circle does not connect these orientations, because an infinite number of great circles can connect

antipodal points on the sphere. The GCDs of the transition trajectories for the PCOH, COH, and ICOH models are equal to π , and are less than π in the NPM and EPC models.

Of the models listed in Table 1, only the NPM model is capable of reproducing the asymmetric EA excursion observed in the leading outrider of PSR B0329+54. The asymmetric EA excursion and offset between m_t and $m = 0$ in the model arise because the nonorthogonality of the mode polarization vectors is a mechanism that breaks the symmetry of the mode transition. The other models do not include a symmetry-breaking mechanism. An asymmetry can be introduced in the EPC model by allowing the PA of the EPC, ψ_e , to be something other than $\pi/4$, which would increase the number of model parameters from $N = 3$ to $N = 4$.

By construction, the orientation of the EPC’s polarization vector in the EPC model is the same as that of the coherent component in the PCOH model. However, the two models are not the same, because the intensity of the EPC is independent of the mode intensities, whereas the intensity of the coherent component in the PCOH model is dependent upon them.

The polarization fractions of the models are compared in Figure 6. The figure is adopted from Figure 2 of Cheng & Ruderman (1979) and Figure 5 of M24. For models that assume the emission is comprised solely of the polarization modes, the polarization fraction is confined to the region defined by the inverted triangle in the figure. The top horizontal boundary at $p = 1$ is formed by coherent polarization modes and the lower diagonal boundaries are formed by incoherent OPMs with intensities that do not randomly vary. With one exception, the polarization fractions are displayed using the same value of the minimum polarization fraction, $p_m = 0.113$. The polarization minima increase as C and ε increase and as $\cos(2\delta_V) \cos(2\delta_L)$ decreases. The overall polarization fractions retain their hyperbola-like shapes as the model parameters change. The figure shows very little difference between the polarization fractions of the NPM, EPC, and PCOH models over the range of $m = \pm 0.1$ ($0.82 < M < 1.22$). In fact, the functional forms of the polarization fractions for the NPM and PCOH models (Equations 20 and 39) are mathematically the same, with $t^2(C) = 2/K_1$. This, in turn, means the physical properties of a mode transition cannot be uniquely determined on the basis of the polarization fraction alone. The polarization fraction of the EPC model extends beyond the boundary indicated by the inverted triangle, because the model includes an EPC in addition to the polarization modes. The polarization fraction at the beginning and end of the EPC mode transition is given by Equation 33 with $m = 1$. The polarization fraction of the COH model remains constant at $p = 1$, which is generally inconsistent with what is observed in individual pulsars and across the pulsar population (e.g., see Figures 3 and 9 of OKJ).

7. EFFECTS OF MODE INTENSITY FLUCTUATIONS

The preceding analyses have generally assumed the mode intensities do not randomly vary. However, the radio emission has long been known to fluctuate (e.g., Ekers & Moffet 1969; Manchester, Taylor, & Huguenin 1975; Backer & Rankin 1980; S84), and the observed switching between orthogonally polarized states is generally regarded as a stochastic process (Cordes, Rankin, & Backer 1978). A model that hopes to replicate the results of single-pulse polarization observations (e.g., S84 and ES04), such as the modulation index of the total intensity, the eigenvalues and eigenvectors of the Stokes QUV covariance matrix, and distributions of the PA, EA, and fractional polarization, should incorporate intensity fluctuations. MS incorporated the fluctuations as a fundamental component in their statistical model of incoherent OPMs.

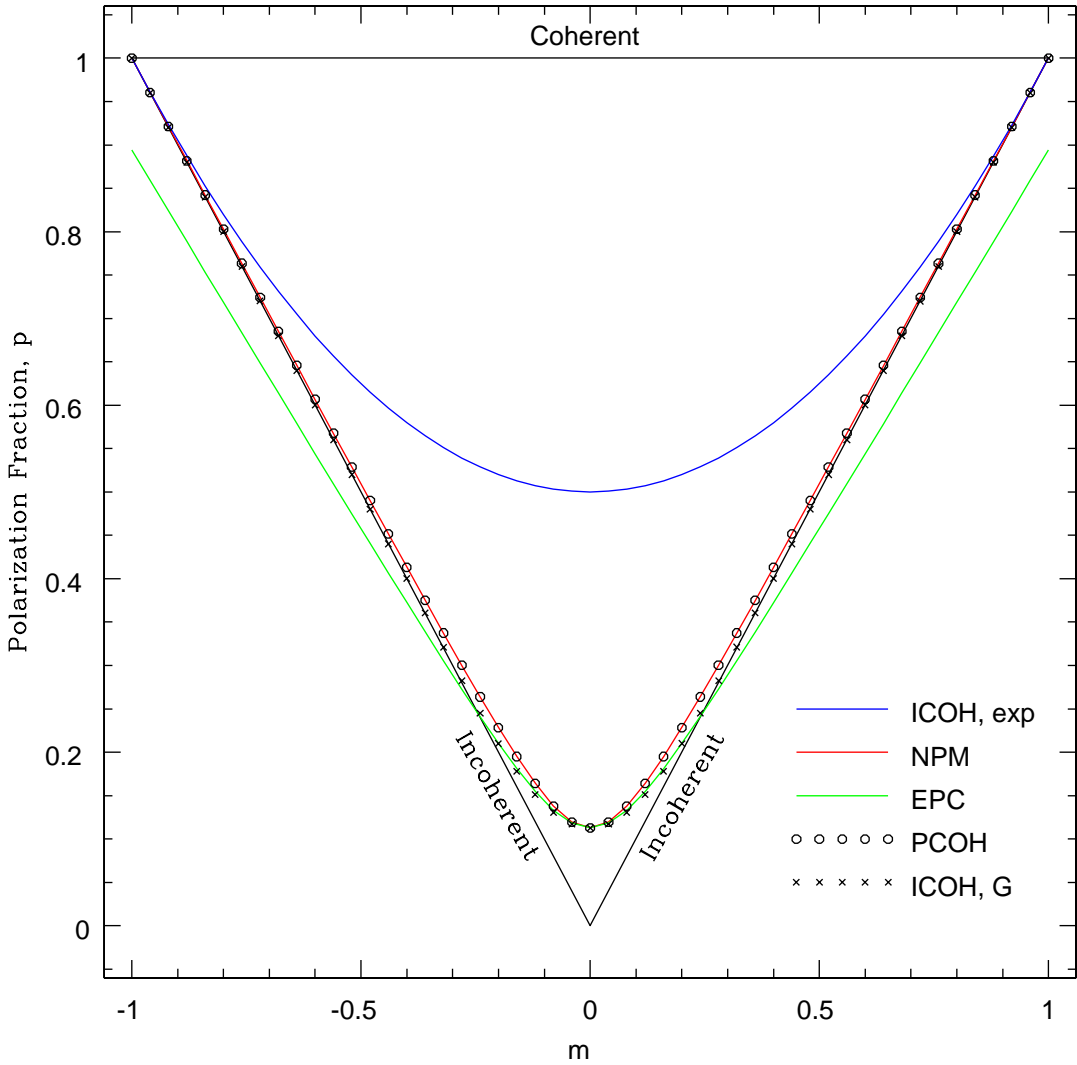


Figure 6. Comparison of model polarization fractions, $p(m)$. The red line is $p(m)$ for the NPM model (Equation 20 with a cosine product of $\cos(2\delta_V)\cos(2\delta_L) = 0.975$), and the open circles represent $p(m)$ for the PCOH model (Equation 39 with a coherence factor of $C = 0.263$). The green line is $p(m)$ for the EPC model (Equation 33 with $\varepsilon = 0.113$), and the black crosses represent $p(m)$ produced by Gaussian fluctuations in incoherent OPM intensities (Equation 41 with a modulation index of $\beta = 0.141$). The blue line is $p(m)$ produced by exponential fluctuations in incoherent OPM intensities (Equation 40). With the exception of the exponential fluctuation case, the minimum polarization fraction for each model is $p_m = 0.113$.

7.1. Polarization Fraction from Fluctuations in Incoherent OPM Intensities

The mode intensity fluctuations contribute to the polarization fraction, and the contribution is dependent upon the statistical character of the fluctuations. As shown by Equation 18 of M22, the

polarization fraction¹ resulting from exponential fluctuations in the intensities of incoherent OPMs is

$$p(m) = \frac{M^2 + 1}{(M + 1)^2} = \frac{1 + m^2}{2}. \quad (40)$$

Equation 40 is shown by the blue line in Figure 6. Its minimum polarization fraction is $p_m = 0.5$, demonstrating that the contributions of the intensity fluctuations to the polarization fraction can be significant. The modulation index, β , varies over the transition from $\beta = 0.71$ at $m = 0$ to $\beta = 1$ at $m = \pm 1$ (see Equation 20 and Figure 2 of M24).

For Gaussian fluctuations in mode intensities, the polarization fraction from Equation 45 of M24 is

$$p(m) = \beta \sqrt{\frac{2}{\pi}} \exp\left(-\frac{m^2}{2\beta^2}\right) + \operatorname{erf}\left(\frac{m}{\beta\sqrt{2}}\right) m, \quad (41)$$

where $\operatorname{erf}(x)$ is the error function. The modulation index is constrained by $\beta \leq 1/(5\sqrt{2}) = 0.141$ to ensure the mode intensities are non-negative (see Equation 40 of M24 and its supporting text). For simplicity and illustration purposes, the total intensity of the emission, the standard deviation of the mode intensities, and thus the modulation index are assumed to be constant across the transition. Equation 41 with $\beta = 0.141$ is shown by the black crosses in Figure 6. Since $\beta = 0.141$ is the largest it can be for Gaussian intensity fluctuations, the polarization minimum can be no larger than $p_m = 0.113$. This is the constraint that sets the value of p_m for the model comparison in the figure. The polarization fraction produced by Gaussian fluctuations in mode intensities replicates that of the EPC model over the range $m = \pm 0.25$. Polarization fractions produced by other types of intensity fluctuations can occupy the $m - p$ parameter space delimited by the exponential and Gaussian examples shown in the figure (see Figure 5 of M24). The examples show that the polarization fraction produced by incoherent OPMs with fluctuating intensities can mimic the polarization produced by more complex models that assume the mode intensities do not fluctuate. Oswald et al. (2023a) assert that the polarization is always equal to zero at a transition between incoherent OPMs and attribute any residual polarization to propagation effects. The polarization is equal to zero only when the OPM intensities are equal and do not randomly vary.

7.2. EA from Fluctuations in Incoherent OPM Intensities

The average EA is calculated from the mean linear polarization, $\langle L \rangle$. Since the fluctuations in the mode intensities contribute to $\langle L \rangle$, the measured EA also depends upon the statistical character of the mode intensity fluctuations. The EA produced by randomly fluctuating OPMs can be determined by selecting a probability distribution for the mode intensities, deriving the mean circular and linear polarization of the combined radiation, and calculating the EA from Equation 7. M22 and M24 derived the mean linear polarization normalized by the mean total intensity, $\bar{L} = \langle L \rangle / \langle I \rangle$, for a variety of mode intensity probability distributions. Those results can be used to calculate the EA by replacing $\langle V \rangle / \langle L \rangle$ in Equation 7 with \bar{V} / \bar{L} , where $\bar{V} = \langle V \rangle / \langle I \rangle$ is the mean circular polarization normalized by the mean total intensity. From Equations 1 and 4, and regardless of the statistical

¹ M22 and M24 refer to Equations 40 and 41 as the normalized mean of linear polarization or the fractional linear polarization. The equations also represent the polarization fraction, as used here, because M22 and M24 assumed the modes are completely linearly polarized.

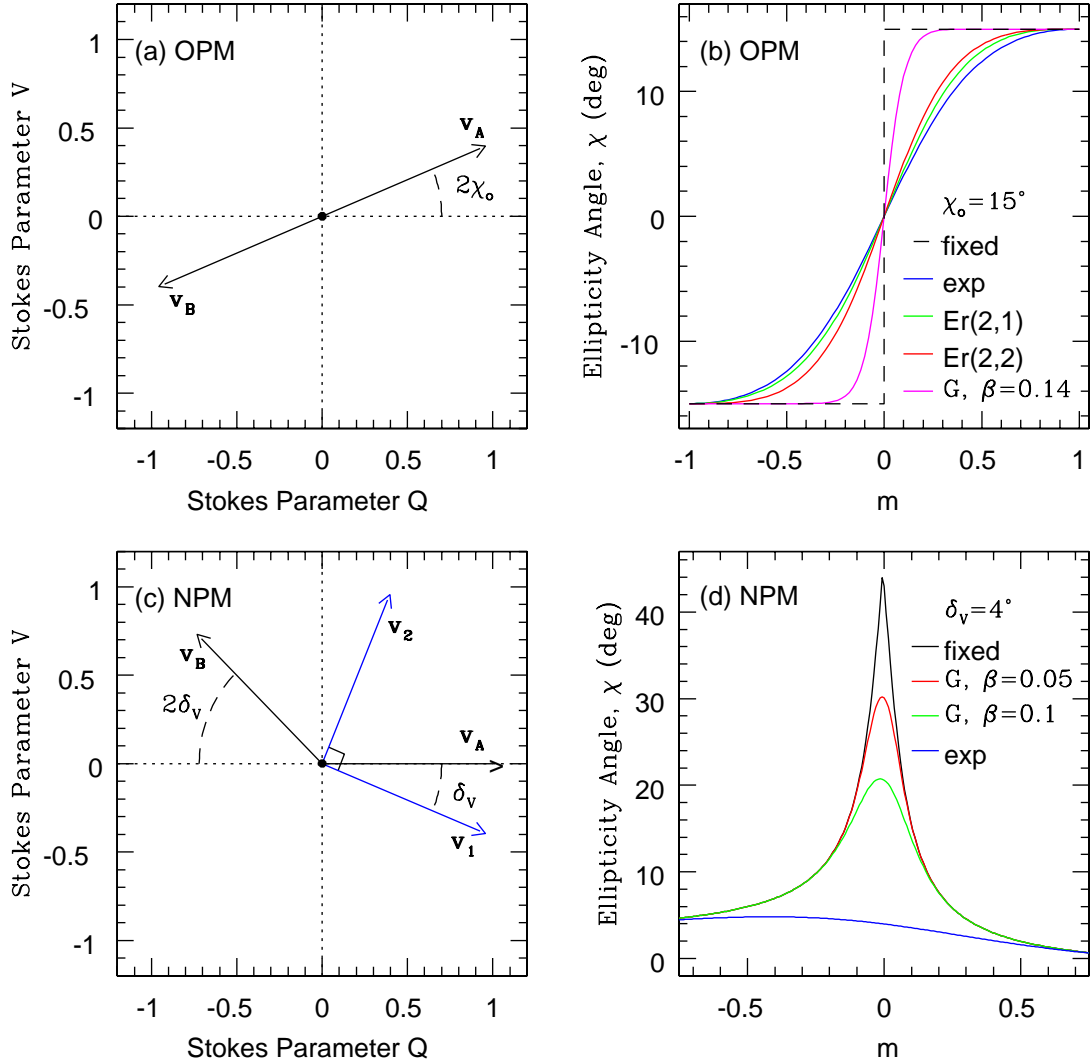


Figure 7. Change in the EA at OPM and NPM transitions when the mode intensities are fixed or RVs. Panel (a) shows the polarization vectors of the OPMs, \mathbf{v}_A and \mathbf{v}_B . Panel (b) shows the measured EA at an OPM transition when the mode intensities are fixed or exponential (exp), Erlang (Er), or Gaussian (G) RVs. Panel (c) compares the unit vectors of the NPMs with two of the eigenvectors of the QUV covariance matrix, \mathbf{v}_1 and \mathbf{v}_2 . Panel (d) shows the measured EAs when the NPM intensities are fixed or exponential or Gaussian RVs.

character of the mode intensity fluctuations, the normalized mean of the circular polarization is always $\bar{V} = m \sin(2\chi_o)$, where χ_o is shown by the OPM vector geometry illustrated in Figure 7(a). For OPM intensities that are exponential RVs, the normalized mean of the linear polarization is Equation 40 multiplied by $\cos(2\chi_o)$, and the EA as a function of m is

$$\chi(m) = \frac{1}{2} \arctan \left[\frac{2m \tan(2\chi_o)}{1 + m^2} \right]. \quad (42)$$

The same procedure can be used to derive the EA produced by other types of OPM intensity distributions. Examples for Gaussian and Erlang OPM intensities are listed in Appendix A, and are compared with the EAs expected from fixed and exponential mode intensities in Figure 7(b). When the OPM intensities are fixed, the EA changes discontinuously by $\Delta\chi = 2\chi_o$ at the mode transition ($m = 0$). When the OPM intensities are random, the EA changes gradually and continuously from that of one mode to the other. The EA transition for Gaussian mode intensities is more acute than the transition resulting from exponential mode intensities. Since the modulation index of a Gaussian RV is less than an exponential RV's, the figure shows the EA transitions becoming more acute as the modulation index decreases. The EAs for the Erlang distributions are shown in the figure to illustrate how the EA changes at a transition when the mode intensity distributions are not the same. The red curve labeled Erlang(2,2) (Equation A3) is the EA resulting from both modes having the same Erlang distribution with their orders equal to 2 ($n_a = n_b = 2$; see Appendix A for the definition of n). The green curve labeled Erlang(2,1) (Equation A4) is the EA resulting from different Erlang distributions with $n_a = 2$ and $n_b = 1$. The EA transitions are antisymmetric about $m = 0$ when the mode intensity distributions are identical, and are asymmetric about $m = 0$ when the distributions are different. More specifically, the behavior of the EA near $m = 1$ in the Erlang(2,1) case approaches that of the Erlang(2,2) case, and approaches the exponential case, which is Erlang(1,1), near $m = -1$.

7.3. EA from Fluctuations in Incoherent NPM Intensities

The NPM model is modified in this section to illustrate how the mode intensity fluctuations affect the EA at a mode transition. Since the EA behavior derived from fixed mode intensities can be similar for all four models, as summarized in Section 6, the effect of the fluctuations on the EA derived from the other models is likely to be similar. For NPMs with fluctuating intensities, the total excursion of the EA at a mode transition depends upon the statistical character of the mode intensity fluctuations. From Equation 7, for example, $\langle V \rangle$ must exceed $\langle L \rangle$ for the magnitude of the EA to exceed $|\chi| = \pi/8$. This can be difficult to produce, because the polarization fluctuations contribute to $\langle L \rangle$, but not to $\langle V \rangle$. When the mode intensities do not vary or their fluctuations are small, $\langle V \rangle$ can be much larger than $\langle L \rangle$, and the EA will be $\chi = \pm\pi/4$, as shown in Figure 1(d). When the fluctuations are very large, $\langle V \rangle$ will likely be much smaller than $\langle L \rangle$, and the EA will vary gradually by $\Delta\chi = \delta_V$ across the mode transition. When the fluctuations are moderate, such that $\langle V \rangle \approx \langle L \rangle$, the EA will be $|\chi| \approx \pi/8$.

The effect of the NPM fluctuations on the EA can be quantified by repeating the analysis of Section 3.2, where $\delta_L = 0$, while allowing the mode intensities to be random instead of fixed. For the NPM vector geometry shown in Figure 7(c), where $\chi_o = 0$, and assuming the NPM intensities are exponential RVs, the measured EA varies with m according to

$$\chi(m) = \frac{1}{2} \arctan \left[\frac{2 \tan \delta_V (1 - m)(1 + m \tan^2 \delta_V)}{(1 + m^2)(1 + \tan^4 \delta_V) + 4m \tan^2 \delta_V} \right]. \quad (43)$$

The transition still occurs at $m_t = -\tan^2 \delta_V$, where the EA is $\chi = \delta_V$.

For NPM intensities that are Gaussian RVs, the EA varies with m as

$$\chi(m) = \frac{1}{2} \arctan \left\{ \frac{\tan \delta_V (1 - m)}{\sqrt{2(1 + \tan^4 \delta_V)}} \frac{\sqrt{\pi}}{\{\beta \exp[-(f(m)/\beta)^2] + f(m) \operatorname{erf}[f(m)/\beta]\} \sqrt{\pi}} \right\}, \quad (44)$$

where $f(m)$ is

$$f(m) = \frac{m + \tan^2 \delta_V}{\sqrt{2(1 + \tan^4 \delta_V)}}. \quad (45)$$

Panel (d) of Figure 7 compares the behavior of the EA at a transition between NPMs when the mode intensities are fixed and random. The black line in the panel is the EA calculated from Equation 19 for fixed mode intensities with $\delta_L = 0$. The red and green lines show the EAs calculated from Equation 44 for Gaussian mode intensities with different modulation indices, as indicated in the panel. The blue line in the panel is the EA calculated from Equation 43 for exponential mode intensities. The figure shows the excursions in EA become more suppressed as the intensity modulation index increases.

7.4. Numerical Simulation of an Incoherent NPM Transition

A numerical simulation was developed to illustrate the effects of mode intensity fluctuations upon the trajectory of an NPM transition across the Poincaré sphere. The simulation generated 10,000 samples for each of the Stokes parameters Q, U, and V. The mode intensities were Gaussian RVs with identical standard deviations, $\sigma_A = \sigma_B = 3$. The mean of the mode B intensity was held constant at $\mu_B = 30$, while the mean of mode A was varied to produce results at different values of m . The PA and EA of mode A were held constant at $\psi_A = \chi_A = 0^\circ$. The PA and EA of mode B were held constant at $\psi_B = \pi/2 - \delta_L$, with $\delta_L = 3^\circ$, and $\chi_B = \delta_V = 6^\circ$. From Equation 18, the mode transition for these values of δ_L and δ_V occurs at about $m_t = -0.0138$. Instrumental noise was included in the simulation with a value of $\sigma_N = 1$. The results of the simulation are shown by the Lambert equal-area projections in the four panels of Figure 8 for different values of m . The most striking feature of all four examples is the data points are not concentrated at one location on the sphere, but are instead dispersed along a mean trajectory between the orientations of the mode polarization vectors. The mean trajectory is similar to those illustrated in Figure 3. The dispersion of the data points along and about the trajectory is caused primarily by the mode intensity fluctuations and, to a much lesser extent, by the instrumental noise. The overall trajectory becomes more apparent near the mode transition, m_t . Panel (a) in the top left corner of the figure shows the result of the simulation when $m = 0.1$ ($\mu_A = 36.67$). The view of the Poincaré sphere is along its Q-axis. The orientation of the mode A polarization vector is located at the center of the projection. As with the other three examples in the figure, the vast majority of data points generated by the simulation reside within one hemisphere of the sphere. While mode A is the primary (dominant) mode for this value of m , the contours are spread about PAs and EAs that are significantly different from those of mode A. The contours in the projection trace the beginnings of an arc that ventures closer to the sphere's right circular pole than to its equator. Panel (b) in the top right corner of the figure shows the result of the simulation when $m = 0$ ($\mu_A = 30$). The view of the sphere in this example is along its U-axis. The overall trajectory of the transition is more apparent because the value of m in the projection is very close to m_t . Mode A remains the primary mode because $m > m_t$. The contours also indicate mode A is the primary, because more data points reside on the left side of the projection than the right. The average EA is near its maximum in this example. Panel (c) in the bottom left corner of the figure shows the result of the simulation when $m = -0.05$ ($\mu_A = 27.14$). The view of the sphere is again along its U-axis. Mode B is now the primary mode because $m < m_t$. The contours follow an arc descending toward the orientation of the mode B polarization vector. Panel (d) in the bottom right corner of the figure shows the result of the simulation when $m = -0.1$ ($\mu_A = 24.54$). The view

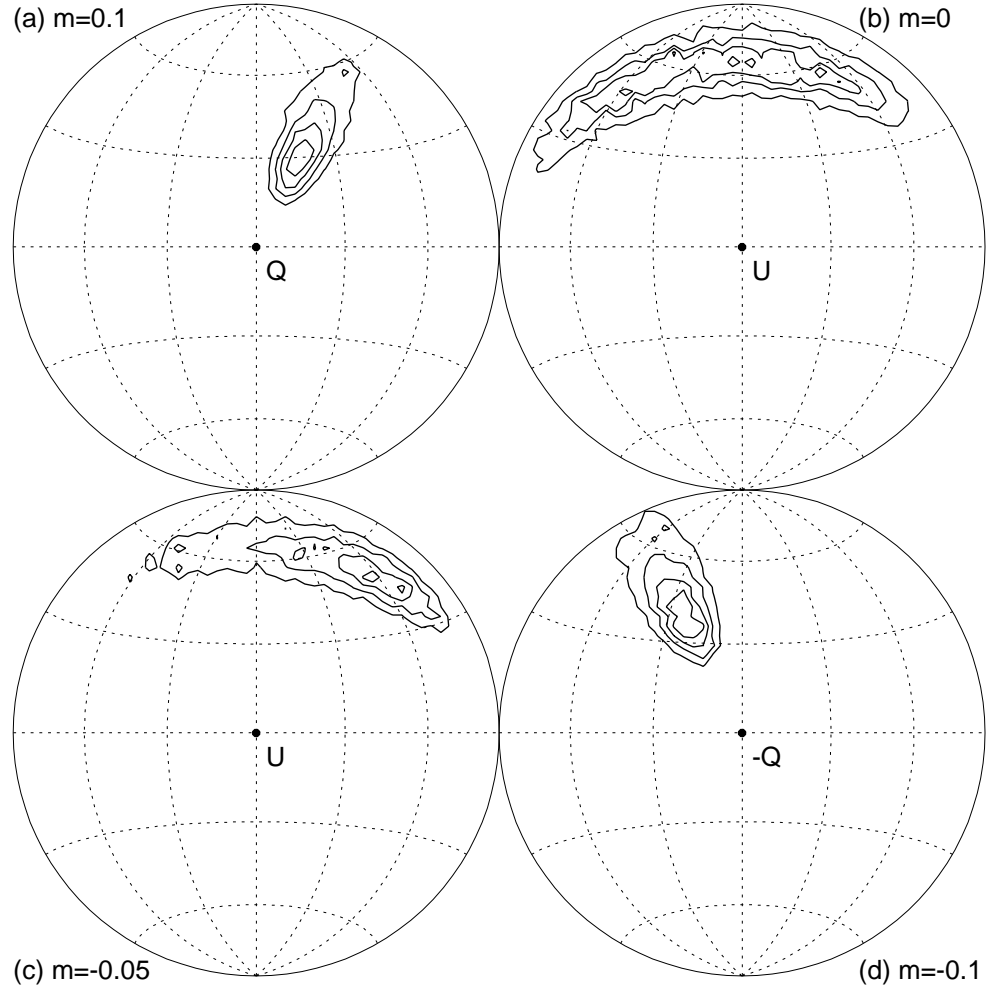


Figure 8. Numerical simulations of the trajectory of an NPM transition on the Poincaré sphere when the mode intensities fluctuate. Each panel shows the result of a simulation for different values of m , as annotated in the figure. The labeled dot at the center of each panel denotes the viewpoint of the sphere's projection. The constant angles used to produce the figure are $\chi_o = 0^\circ$, $\delta_L = 3^\circ$ and $\delta_V = 6^\circ$. The contour levels are 0.2, 0.4, 0.6, and 0.8 of the peak value in each projection. See the text for a detailed explanation of the simulations.

of the sphere is now along its $-Q$ -axis. Mode B is the primary mode for this value of m , but the contours are spread about PAs and EAs that are significantly different from those of mode B. The contours begin to coincide with the orientation of the mode B vector as m approaches $m = -1$.

Another numerical simulation was developed to investigate how fluctuations in δ_L and δ_V might affect the transition trajectory. This modification effectively enabled multiple trajectories between the orientations of the mode vectors, thereby dispersing the polarized signal across the surface of the Poincaré sphere and diluting the pattern of the arc. The results of this simulation are not shown.

7.5. Eigenvalues of the Stokes QUV Covariance Matrix

The origin of the polarization fluctuations can be investigated by examining the size and shape of the data point cluster formed from multiple samples of the Stokes parameters Q, U, and V recorded at a given pulse longitude (McKinnon 2004, hereafter M04). The size and shape of the cluster can be quantified by computing the eigenvalues of the QUV covariance matrix (M04; ES04). The measured eigenvalues (e.g., Figure 3 of ES04 and Figure 3 of Edwards (2004)) can then be compared with the eigenvalues derived from the polarization models.

The eigenvalues for the general case of the NPM model, where departures from orthogonality occur in both linear and circular polarization, can be derived by following the analysis outlined in Section 2.4 of M04. For consistency, the PAs and EAs of the mode polarization vectors used in the derivation are the same as those used in Section 3.3. The variances of the mode intensities are assumed to equal one another, $\sigma_A^2 = \sigma_B^2 = \sigma^2$, to simplify the analysis and to focus the result on the effects of the vector geometry. The resulting eigenvalues are

$$\tau_1 = \sigma_N^2 + \sigma^2[1 + \cos(2\delta_V) \cos(2\delta_L)], \quad (46)$$

$$\tau_2 = \sigma_N^2 + \sigma^2[1 - \cos(2\delta_V) \cos(2\delta_L)], \quad (47)$$

$$\tau_3 = \sigma_N^2, \quad (48)$$

where σ_N is the magnitude of the instrumental noise. The eigenvalues are generally not equal to one another, indicating the QUV data point cluster does not possess an axis of rotational symmetry (M04). The first eigenvalue is larger than the other two. The third eigenvalue is the square of the instrumental noise. The second and third eigenvalues are equal when the polarization modes are orthogonal ($\delta_L = \delta_V = 0$) and are approximately equal when the departures from orthogonality are small ($\delta_L, \delta_V \ll 1$).

The eigenvectors associated with the eigenvalues are not the same as the mode polarization vectors, because the eigenvectors are orthogonal, but the mode vectors are not. Panel (c) of Figure 7 compares the unit vectors of the NPMs, \mathbf{v}_A and \mathbf{v}_B , with two of the eigenvectors of the QUV covariance matrix, \mathbf{v}_1 and \mathbf{v}_2 . The third eigenvector, \mathbf{v}_3 , is perpendicular to the plane of the figure. The panel shows the magnitude of the EA for the first eigenvector is half the difference between the EAs of the mode A and B vectors. A quantitative comparison between the eigenvectors and mode vectors is made in Appendix B.

8. DISCUSSION

8.1. EA Excursion by Vector Rotation

D20 produced an EA excursion by rotating a polarization vector across the Poincaré sphere. He posited a “polarization patch” located in the equatorial plane of the sphere near, but not on, its U-axis (i.e., the DWI mixing angle was $\psi_{mx} \sim \pi/4$). The single patch is consistent with his assumption of coherent modes and a polarization vector with fixed amplitude and modest signal-to-noise ratio. D20 then rotated the patch about the Q-axis by approximately π radians. The rotation is equivalent to changing the mode phase lag, δ_{ox} , in DWI’s COH model. The maximum value of the EA resulting from the vector rotation approaches $\chi \sim \pi/4$, and the total change in PA is slightly less than $\pi/2$.

He then discusses the apparent similarities between the vector rotation and a mode transition, but he makes clear that the two mechanisms are not the same. D20 does not cite the physical process responsible for the vector rotation, but it is consistent with Generalized Faraday Rotation (GFR), where the vector rotates on a small circle of the Poincaré sphere about a sphere diagonal defined by the mode polarization vectors (Kennett & Melrose 1998). The vector rotation is also consistent with the Faraday pulsation model of Cocke & Pacholczyk (1976). The vector rotation produced by GFR is not limited to π , and can range from 0 to in excess of 2π . The angular radius of the small circle can range from 0 to $\pi/2$ ($0 \leq \psi_{mx} \leq \pi/4$), causing the total change in PA to be as small as $\Delta\psi = 0$ or as large as $\Delta\psi = \pi/2$ and the maximum value of the EA to range from 0 to $\pi/4$, depending upon the angular offset between the polarization vector and the mode diagonal.

Similarly, OKJ used their PCOH model to show that the EA excursion in PSR J1157-6224 is consistent with the rotation of the polarization vector at constant C and R . The coherence factor and mode strength ratio were derived from the near-constant value of the polarization fraction at the EA excursion and the maximum value of the EA. Their analysis showed the mode phase offset, η , varied linearly with pulse longitude. Both D20 and DWI predicted the phase offset might vary in this way. OKJ also found that the EA of PSR J0820-1350 changed with wavelength while its polarization fraction remained constant. Again assuming that R and C remained constant, they showed the mode phase offset varied with wavelength as either λ^2 or λ^3 . Lower et al. (2024) demonstrated that changes in the polarization angles of the radio magnetar XTE J1810-197 are consistent with a frequency-dependent rotation of its polarization vector. The EPC model can also produce a vector rotation by holding m and ε constant while allowing the EA of the EPC, χ_e , to vary.

8.2. Potential Model Applications

8.2.1. Orientation Angles of the Polarization Vector in PSR B0809+74

The NPM model is qualitatively consistent with the polarization properties of PSR B0809+74 at 328 MHz (Figure 2 of Edwards (2004)). The observation shows polarization modes occurring across most of its pulse profile. The PA traces of the two modes are approximately parallel and vary linearly with negative slopes across the pulse. Ramachandran et al. (2002) analyzed the same data set as Edwards (2004) and found the PA separation between the traces was not equal to 90° . The average PA bridges the two traces via a gradual transition near the pulse center. The modes are likely responsible for the low polarization observed across the pulse. A depression in the polarization is coincident with the PA transition. The average EA consists of a broad, asymmetric feature that extends conspicuously over the same range of pulse longitude as the PA transition. The feature peaks at $\chi \simeq 32^\circ$ and is aligned in pulse longitude with the PA transition.

Figure 9 is an attempt to replicate the observed behavior of the pulsar's PA and EA using the equations derived for them in Section 3.3. The solid line in the top panel of the figure shows the average PA calculated from Equation 21, with the PA of mode A varying linearly with m , ($\chi_o(m) = K_0 m$). The PA traces of the two modes are shown by the dashed lines in the panel. The PA trace of mode B is offset from the trace of mode A by $\pi/2 - |\delta_L|$. The solid line in the bottom panel of the figure shows the average EA calculated from Equation 19. The dashed line in the panel denotes the EA of mode A, χ_o . The values of K_0 , χ_o , δ_L , and δ_V used to calculate the PA and EA are annotated in the figure. The qualitative agreement between the calculated and observed angles is good. The calculated PA replicates the gradual PA transition that connects the PA traces of the

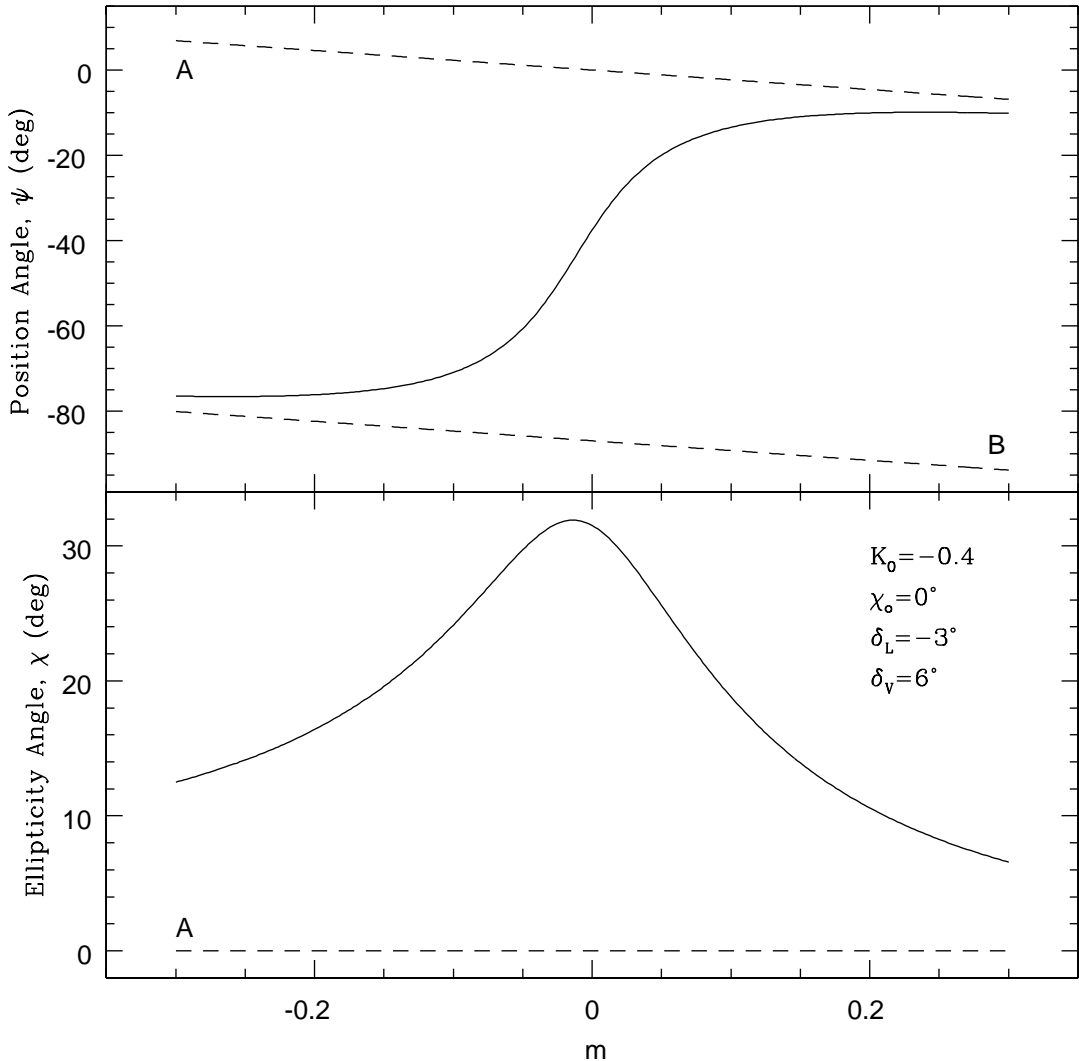


Figure 9. Model of the PA and EA in PSR B0809+74 assuming the mode polarization vectors are not orthogonal. The solid line in the top panel shows the PA as calculated from Equation 21. The dashed lines denote the PA traces of the individual polarization modes, A and B. The solid line in the bottom panel denotes the EA as calculated from Equation 19. The dashed line represents the EA of mode A.

individual polarization modes. The calculated EA reproduces the asymmetry, longitudinal extent, and peak value of the observed EA.

8.2.2. The Polarization Annulus in PSR B0329+54

Each model of a mode transition is capable of producing a polarization arc on the Poincaré sphere, and it is tempting to attribute the partial annulus observed in PSR B0329+54 (Figure 2 of ES04) to one or more of the models. However, the mode transition interpretation is not consistent with the observed annulus, because the models require the orientations of the mode polarization vectors to reside at either end of the polarization arc, whereas the symmetry axis of the observed annulus appears to be aligned with one of the mode vectors (i.e., the mode vectors of the models appear to

be perpendicular to the observed mode vectors). ES04 attribute the annulus to GFR. In its simplest form, GFR requires the modes to be coherent, and it would appear as a well-defined arc on the Poincaré sphere, with the radial spread of the arc determined by the polarization signal-to-noise ratio (e.g., see Figure 3 of Kennett & Melrose 1998). The observed annulus, however, is diffuse, and GFR by itself cannot reproduce the compact ellipse observed at the center of the other hemisphere of the sphere. Melrose et al. (2006) developed a numerical simulation that reproduced the observation. The simulation incorporated superposed NPMs with slightly correlated mode intensities and randomly varying orientations. To reproduce both the compact ellipse and the annulus, one of the modes had to be completely absent in a significant fraction of pulses. Melrose et al. (2006) mention that GFR is complementary to their model, but they stress that their model requires the data points within the annulus to be weakly polarized, whereas there is no such implication for GFR. The mode transitions produced by the NPM, EPC, and PCOH models support their interpretation of a weakly polarized annulus. (The NPM model is essentially an analytical version of the NPM transition that is part of their numerical simulation; see Figure 8(b)). Another interpretation of the partial annulus and compact ellipse is a stochastic version of the PCOH model. In this interpretation, the compact ellipse would represent the model's incoherent component and the partial annulus would represent its coherent component. Since the polarization fraction of the incoherent component is independent of C and η , its position remains fixed on the sphere. Fluctuations in the mode intensities, which are equivalent to fluctuations in R , cause polarization data points to fall within either hemisphere of the Poincaré sphere. The polarization of the coherent component depends upon the phase offset, η , and fluctuations in η will cause its polarization vector to rotate about an axis defined by the polarization vector of the incoherent component. The angular extent of the annulus would then depend upon the standard deviation of the η fluctuations.

9. SUMMARY

Four models of pulsar polarization were examined to quantify and understand the behavior of a polarization vector's PA and EA at a transition between polarization modes. The results of each model show the PA can change gradually, instead of discontinuously, at a mode transition, and the EA can trace an excursion that originates near the equator of the Poincaré sphere and passes near one of its poles. The results of the models can be similar to one another, indicating that the interpretation of an observed mode transition within the context of a particular model may not be unique. For example, the variations in the polarization fractions across a transition that are predicted by the models can resemble one another and in some cases are identical. For each model, the trajectory of a transition on the Poincaré sphere follows a great circle geodesic that connects the orientations of the mode polarization vectors. In contrast, the change in PA and EA caused by a vector rotation (e.g., via GFR) follows a small circle on the sphere. The COH, PCOH, and EPC models can account for changes in the polarization angles due to a vector rotation, in addition to a mode transition. Only the NPM model and an enhanced version of the EPC model can produce an asymmetric EA excursion about a PA transition, as observed in PSR B0329+54.

The effects of mode intensity fluctuations upon the polarization properties of a mode transition were investigated. At a pulse longitude where the mean values of the fluctuating mode intensities are approximately equal, individual PA-EA pairs can take on a wide range of values constrained by the transition trajectory, forming a polarization arc on the Poincaré sphere. The polarization fraction and average EA depend upon the statistical character of the intensity fluctuations. The polarization

fraction increases with the intensity fluctuations. An EA excursion can be large when the mode intensities are quasi-stable and is suppressed when the intensity fluctuations are large.

ACKNOWLEDGMENTS

I thank an anonymous referee for constructive comments that improved the manuscript. The National Radio Astronomy Observatory is a facility of the National Science Foundation operated under cooperative agreement by Associated Universities, Inc.

APPENDIX

A. ELLIPTICITY ANGLES FROM GAUSSIAN AND ERLANG OPM INTENSITIES

Figure 7(b) compares changes in the measured EA at an incoherent OPM transition for different types of mode intensity fluctuations. The equations for the EAs shown in the figure for Gaussian and Erlang fluctuations are listed in this appendix.

For OPMs with Gaussian intensities, the normalized mean of the linear polarization is Equation 41 multiplied by $\cos(2\chi_o)$, and the normalized mean of the circular polarization is $\bar{V} = m \sin(2\chi_o)$. The EA from Equation 7 is

$$\chi(m) = \frac{1}{2} \arctan \left[\frac{m \tan(2\chi_o) \sqrt{\pi}}{\beta \exp(-m^2/2\beta^2) \sqrt{2} + \text{erf}(m/(\beta\sqrt{2})) m \sqrt{\pi}} \right]. \quad (\text{A1})$$

Equation A1 is shown by the magenta line in Figure 7(b).

The linear polarization resulting from mode intensities that are Erlang RVs was derived in M24. For reference, the Erlang distribution is

$$f(x, \mu, n) = \frac{x^{n-1}}{\Gamma(n)\mu^n} \exp\left(-\frac{x}{\mu}\right), \quad x \geq 0, \quad (\text{A2})$$

where μ is a positive scaling factor, n is a positive integer representing the order of the distribution, and $\Gamma(n) = (n-1)!$ is the gamma function. The general equation for \bar{L} for Erlang mode intensities is given by Equation 24 of M24. When the orders of the Erlang distributions for OPM intensities are both equal to 2 ($n_a = n_b = 2$), the EA is

$$\chi(m) = \frac{1}{2} \arctan \left[\frac{8m \tan(2\chi_o)}{3 + 6m^2 - m^4} \right]. \quad (\text{A3})$$

Equation A3 is shown by the red line in Figure 7(b).

For Erlang RVs with $n_a = 2$ and $n_b = 1$, \bar{L} can be calculated from Equation 26 of M24. The resulting EA is

$$\chi(m) = \frac{1}{2} \arctan \left[\frac{m(3-m)^2 \tan(2\chi_o)}{4 - 3m(1-m)^2} \right]. \quad (\text{A4})$$

Equation A4 is shown by the green line in Figure 7(b).

B. EIGENVECTORS OF THE STOKES QUV COVARIANCE MATRIX

As noted in Section 7.5, the eigenvectors of the Stokes QUV covariance matrix are generally not the same as the mode polarization vectors. This can be demonstrated using the vector geometry shown in Figure 7(c), where the mode vectors deviate from orthogonality in circular polarization only. The unit vectors for the polarization modes shown in the figure are

$$\mathbf{v}_A = \begin{bmatrix} 1 \\ 0 \\ 0 \end{bmatrix}, \quad \mathbf{v}_B = \begin{bmatrix} -\cos(2\delta_V) \\ 0 \\ \sin(2\delta_V) \end{bmatrix}. \quad (B5)$$

The PA and EA of mode A are $\psi_A = \chi_A = 0$. They are $\psi_B = \pi/2$ and $\chi_B = \delta_V$ for mode B. The eigenvectors associated with the eigenvalues given by Equations 46 - 48 when $\delta_L = 0$ are

$$\mathbf{v}_1 = \begin{bmatrix} \cos \delta_V \\ 0 \\ -\sin \delta_V \end{bmatrix}, \quad \mathbf{v}_2 = \begin{bmatrix} \sin \delta_V \\ 0 \\ \cos \delta_V \end{bmatrix}, \quad \mathbf{v}_3 = \begin{bmatrix} 0 \\ -1 \\ 0 \end{bmatrix}. \quad (B6)$$

The eigenvectors are perpendicular to one another. The first eigenvector, \mathbf{v}_1 , is aligned with the major axis of the QUV data point cluster. Its PA is $\psi_1 = 0$, and its EA is $\chi_1 = -\delta_V/2$. The magnitude of χ_1 is half the difference between the EAs of modes A and B. When the mode vectors are orthogonal ($\delta_V = 0$), the first eigenvector and the mode A polarization vector are identical.

REFERENCES

Allen, M. C. & Melrose, D. B. 1982, Proc. Astron. Soc. Aust., 4, 365

Backer, D. C. & Rankin, J. M. 1980, ApJS, 42, 143

Barnard, J. J. & Arons, J. 1986, ApJ, 302, 138

Cheng, A. F. & Ruderman, M. A. 1979, ApJ, 229, 348

Cocke, W. J. & Pacholczyk, A. G. 1976, ApJ, 204, L13

Cordes, J. M., Rankin, J., & Backer, D. C. 1978, ApJ, 223, 961

Dyks, J. 2020, MNRAS, 495, L118 (D20)

Dyks, J., Weltevrede, P., & Ilie, C. 2021, MNRAS, 501, 2156 (DWI)

Edwards, R. T. 2004, A&A, 426, 677

Edwards, R. T. & Stappers, B. W. 2004, A&A, 421, 681 (ES04)

Ekers, R. D. & Moffet, A. T. 1969, ApJ, 158, L1

Kells, L. M., Kern, W. F., & Bland, J. R., 1940, Plane and Spherical Trigonometry (New York: McGraw-Hill)

Kennett, M. & Melrose, D. 1998, Proc. Astron. Soc. Aust., 15, 211

Lower, M. E., Johnston, S., Lyutikov, M., et al., 2024, Nature, 8, 606

Manchester, R. N., Taylor, J. H., & Huguenin, G. R. 1975, ApJ, 196, 83

McKinnon, M. M. 2003, ApJ, 590, 1026 (M03)

McKinnon, M. M. 2004, ApJ, 606, 1154 (M04)

McKinnon, M. M. 2022, ApJ, 937, 92 (M22)

McKinnon, M. M. 2024, ApJ, 961, 151 (M24)

McKinnon, M. M. & Stinebring, D. R. 1998, ApJ, 502, 883 (MS)

Melrose, D. B. 1979, Aust. J. Phys., 32, 61

Melrose, D. B., Miller, A., Karastergiou, A., & Luo, Q. 2006, MNRAS, 365, 638

Oswald, L. S., Johnston, S., Karastergiou, A., et al. 2023a, MNRAS, 520, 4961

Oswald, L. S., Karastergiou, A., & Johnston, S. 2023b, MNRAS, 525, 840 (OKJ)

Petrova, S. A., 2001, A&A, 378, 883

Radhakrishnan, V. & Cooke, D. J. 1969, Astrophys. Lett., 3, 225

Ramachandran, R., Rankin, J. M., Stappers, B. W., et al. 2002, A&A, 381, 993

Stinebring, D. R., Cordes, J. M., Rankin, J. M., et al. 1984, ApJS, 55, 247 (S84)